

Direct numerical simulation of saturated deformable porous media using parallel hybrid Lattice–Boltzmann and finite element method

Irfan Khan and Cyrus K. Aidun^{*,†}

*G. W. Woodruff School of Mechanical Engineering, Georgia Institute of Technology,
500, 10th Street, Atlanta, GA 30318, U.S.A.*

SUMMARY

Numerical techniques for modeling saturated deformable porous media have mainly been based on mixture theory or homogenization techniques. However, these techniques rely on phenomenological relationships for the constitutive equations along with assumptions of homogeneous and isotropic material properties to obtain closure. Direct numerical simulations of the multiphase problem for flow in deformable porous media avoid such assumptions and thus can provide significantly accurate understanding of the physics involved. They serve as a tool to investigate the constitutive relationships in complex geometries. They also allow the validation of the existing mixture theory models and determine their limitations.

In this work, a parallel hybrid method using Lattice Boltzmann Method (LBM) for fluid phase and Finite Element Method (FEM) for solid phase is used for direct numerical simulation of saturated deformable porous media. The method provides a number of unique features including scalability on distributed computing necessary for such a problem. The method has been validated for modeling fluid–structure interactions in complex geometries against a number of experimental and analytical solutions. Further some challenging problems has been chosen to show the capability of the method. Copyright © 2010 John Wiley & Sons, Ltd.

Received 31 December 2009; Revised 13 October 2010; Accepted 29 October 2010

KEY WORDS: saturated deformable porous media; direct simulation; Lattice–Boltzmann method; finite element method

1. INTRODUCTION

Since the fundamental work by Biot [1, 2] there has been considerable effort in developing rigorous theory that can accurately describe the dynamic behavior of saturated deformable porous media. The Theory of Porous Media (TPM) developed by Bowen [3, 4] de Boer [5, 6] Ehlers [7] Bluhm [8] makes use of fundamental principles of thermodynamic constraints to obtain basic conservation equations with constitutive assumptions that govern the dynamic behavior of saturated porous media. In spite of the rigour, the approach makes assumption about the constitutive relationships, particularly those that govern the behavior of permeability. The resulting governing equations are spatially discretized and solved in a finite element framework. The assumption of a smeared media used in these techniques requires that at any time particles from all the phases occupy a given position. Thus, the governing equations contain material properties of the bulk media as opposed to a single homogeneous phase. Additional experimental work is needed in order to obtain such bulk media parameters. This becomes difficult particularly for non-homogeneous or anisotropic

^{*}Correspondence to: Cyrus K. Aidun, G. W. Woodruff School of Mechanical Engineering, Georgia Institute of Technology, 500, 10th Street, Atlanta, GA, U.S.A.

[†]E-mail: cyrus.aidun@me.gatech.edu

media, where information about a material property as a function of space has to be obtained. However, in a number of fields there is a need to investigate the effects of non-homogeneous and anisotropic saturated porous media (paper manufacturing, etc.).

Direct numerical simulations do not make assumptions about the constitutive relationships in a mixture. Rather, these relationships are the result of a comprehensive model that does not make assumptions of the bulk media. Further, they make use of the readily available material properties of the homogeneous constituent and do not require prior experimental work to obtain the bulk medium parameters. Thus, they model the phenomena in a significantly accurate way and provide substantial understanding of the physics involved. They can be viewed as 'numerical experiments' for detailed understanding of the phenomena. They also serve to validate the existing homogenization models and corroborate them in assumptions of the constitutive relations.

Considerable work has been done in using direct numerical simulations to investigate flows in rigid porous media [9–11]. Boutt *et al.* [12] used a discrete element method coupled with LBM to simulate saturated porous media comprising of rigid movable particles. However, there has been no attempt to carry out direct numerical simulations on deformable saturated porous media. A fully coupled and parallelized numerical method using Lattice–Boltzmann method for fluid phase and finite element method (FEM) for solid phase is used in this research work to perform direct numerical simulations of saturated deformable porous media. The Lattice–Boltzmann method with its simplicity and local nature of calculations is suitable to model complex flows such as flow in porous media (Aidun and Clausen [13]). The FEM has been proven as a robust technique for modeling elastic deformations.

Section 2 describes the methodology including both Lattice–Boltzmann and FEM methods, the LBM-FEM coupling, near contact modeling and parallelization scheme. In Section 3, the method is compared against the experimental and analytical work, to validate its capability in modeling fluid–structure interaction in a complex geometry such as a porous media. In Section 4, some challenging simulation results of flow in model porous media are provided. The paper ends with conclusions and plans for the future.

2. METHODOLOGY

For modeling fluid flow, the Lattice–Boltzmann method (LBM) has evolved as an attractive alternative. The accuracy of LBM has been shown to be comparable to traditional numerical methods such as finite-volume, finite-difference and finite element [14–16]. Further, for solving flows in complex geometries like porous media, the LBM has proved to be more efficient than traditional methods [15]. Owing to the local nature of the calculations, the method is amenable to distributed computing. This feature of LBM is very important for this research work, as the size of the computational domain turns out to be too large to be solved efficiently using serial computing. In this work, the BGK LBM with single-relaxation as implemented in [17] has been used.

In this study, as a first approximation, a linear elastic model has been used for simulating the deformation of saturated porous media. In spite of the assumption, valuable information can be gathered about the behavior of deformable porous media. The FEM with four-node linear quadrilateral elements has been used to discretize the geometry and form the weak system. The reason for using FEM for modeling the deformation of the solid phase is its robustness and accuracy. Further, there has been progress in the development of efficient parallel iterative schemes [18] that make the solution of solid phase easy.

In the following, the LBM and FEM are described in detail including fluid–solid coupling and near contact mechanics. Further, a brief description of parallelization scheme has also been provided.

Lattice–Boltzmann method

The LBM is based on a specialized discretization of the continuous Boltzmann equation. As such, it is a kinetic model that models the fluid phase at a mesoscopic level. The LBM starts with an initial

lattice where each lattice node is characterized by a particle distribution function $f_k(\mathbf{x}^e, t)$. The distribution function gives the probability of finding a particle at position \mathbf{x} , time t and moving in the discrete direction k . The evolution of $f_k(\mathbf{x}, t)$ with time is governed by the Lattice–Boltzmann equation given as

$$f_k(\mathbf{x}^e + \mathbf{e}_k, t + 1) = f_k(\mathbf{x}^e, t) + \frac{1}{\tau} [f_k^{\text{eq}}(\mathbf{x}^e, t) - f_k(\mathbf{x}^e, t)]. \quad (1)$$

Here $f_k^{\text{eq}}(\mathbf{x}^e, t)$ is the equilibrium distribution function at (\mathbf{x}^e, t) , τ is the single relaxation time constant and \mathbf{e}_k is the discrete velocity vector. The fluid density ρ and the macroscopic fluid velocity $\mathbf{v}(\mathbf{x}^e, t)$ are obtained from the first two moments, given by

$$\rho(\mathbf{x}^e, t) = \sum_k f_k(\mathbf{x}^e, t) \quad \text{and} \quad \rho(\mathbf{x}^e, t)\mathbf{v}(\mathbf{x}^e, t) = \sum_k f_k(\mathbf{x}^e, t)\mathbf{e}_k. \quad (2)$$

The most common lattice model for two-dimensional case is D2Q9 model which uses nine discrete velocity directions, while the model for three-dimensional case is D3Q19, which uses cubic lattice with 19 discrete velocity directions [17] for the fluid particles moving along the horizontal, vertical and diagonal links. The equilibrium distribution function is defined as

$$f_k^{\text{eq}} = w_k \rho [1 + 3\mathbf{e}_k \cdot \mathbf{v} + \frac{9}{2}(\mathbf{e}_k \cdot \mathbf{v})^2 - \frac{3}{2}|\mathbf{v}|^2] \quad (3)$$

with $w_0 = 4/9$ for fluid particles at rest, $w_{1-4} = 1/9$ for fluid particles moving in non-diagonal directions, and $w_{5-8} = 1/36$ for diagonal directions in two-dimensional D2Q9 model; and $w_0 = 1/3$, $w_{1-6} = 1/18$ (non-diagonal directions), and $w_{7-18} = 1/36$ (diagonal directions) in three-dimensional D3Q19 model. For the present model, the pseudospeed of sound is $c_s = \sqrt{1/3}$ and the kinematic viscosity is $\nu = (2\tau - 1)/6$. In the longer time scale, the LBM is effectively solving the Navier–Stokes equations. Details of the implementation can be found in [17].

Finite element method

The deformation of the porous structure has been approximated using a linear elastic model. Within the elastic limit, Cauchy's equation governs the transient behavior of deformation inside the solid structure. Cauchy's equation is given as

$$\nabla \cdot \mathbf{T} + \rho \mathbf{g} = \rho \ddot{\mathbf{u}}, \quad (4)$$

where \mathbf{T} is Cauchy's stress tensor, $\rho \mathbf{g}$ is the body force and $\ddot{\mathbf{u}}$ is the resulting acceleration. The weak form of the equation using the Principle of Virtual displacement is given as

$$\int_V [\boldsymbol{\varepsilon}^T \cdot \mathbf{T} + \rho \ddot{\mathbf{u}} \cdot \delta \mathbf{u}] dV = \int_V \rho \mathbf{g} \cdot \delta \mathbf{u} dV + \int_S \hat{\mathbf{t}} \cdot \delta \mathbf{u} dS, \quad (5)$$

where V and S represent the volume and boundary of the domain. $\delta \mathbf{u}$ represents the virtual displacement, \mathbf{T} and $\boldsymbol{\varepsilon}$ represent the stress and strain tensors, respectively and $\rho \mathbf{g}$ and $\hat{\mathbf{t}}$ represent the body and surface forces, respectively.

The geometry has been discretized using four-node tetrahedral elements as shown in Figure 1. Within each element, deformation (\mathbf{u}) is approximated using Lagrangian shape functions as

$$\mathbf{u}(x, y, z) = \sum_{i=1}^n \bar{\mathbf{u}}_i \psi_i(x, y, z), \quad (6)$$

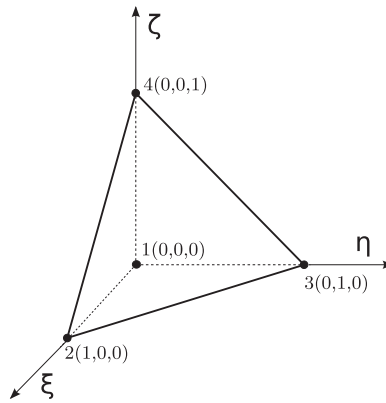


Figure 1. Master tetrahedral element.

where n represents the nodes per element, \bar{u}_i is the value of \mathbf{u} at node i and ψ_i are the Lagrangian shape functions for a tetrahedral element given as

$$\psi_i(\xi, \eta, \zeta) \begin{cases} \psi_1 = 1 - \xi - \eta - \zeta, \\ \psi_2 = \xi, \\ \psi_3 = \eta, \\ \psi_4 = \zeta. \end{cases} \quad (7)$$

The constitutive relations between stress and strain, the compatibility relations of linear elasticity and the equations for the approximation of \mathbf{u} are substituted in the weak form given by Equation (5). Subsequently, the boundary conditions and the condition of continuity of solution are applied resulting in a system given as

$$[M]\{\ddot{\mathbf{u}}\} + [C]\{\dot{\mathbf{u}}\} + [K]\{\mathbf{u}\} = \{\mathbf{f}\}, \quad (8)$$

where $[M]$ is the mass matrix, $[C]$ is the damping matrix, $[K]$ is the stiffness matrix, $\{\mathbf{f}\}$ is the force vector and $\{\mathbf{u}\}$ is the displacement vector.

The Rayleigh damping matrix is used to construct the damping matrix $[C]$, given as follows:

$$[C] = \alpha_r[M] + \beta_r[K]. \quad (9)$$

The coefficients α_r and β_r are related to the solid body damping ratios via $\zeta(\omega_n) = 0.5(\alpha_r\omega_n^{-1} + \beta_r\omega_n)$, where ζ is the damping ratio for the given modal circular frequency ω_n . The Rayleigh damping coefficients are chosen based on the desired damping ratios for the given solid material properties. To avoid influencing the dynamics of the porous media, damping ratios are chosen such that $\zeta(\omega_n) \ll 1$ for all simulations presented here, except when mentioned otherwise.

To integrate the second-order system of equations in time, Newmark's scheme is adopted. The deformation and its derivatives for time $t+1$ are approximated using their values at time t as follows:

$$\{\mathbf{u}\}_{t+1} = \{\mathbf{u}\}_t + \Delta t\{\dot{\mathbf{u}}\}_t + \frac{\Delta t^2}{2}[(1-2\beta)\{\ddot{\mathbf{u}}\}_t + 2\beta\{\ddot{\mathbf{u}}\}_{t+1}], \quad (10)$$

$$\{\dot{\mathbf{u}}\}_{t+1} = \{\dot{\mathbf{u}}\}_t + \Delta t[(1-\gamma)\{\ddot{\mathbf{u}}\}_t + \gamma\{\ddot{\mathbf{u}}\}_{t+1}], \quad (11)$$

where Δt is the timestep and γ, β are Newmark's integration constants that determine the stability and accuracy of the scheme. We choose $\gamma=0.5$ and $\beta=0.25$ resulting in a constant-average acceleration method that is unconditionally stable.

Substituting Equations (10) and (11) into the system of equations given by Equation (8) and evaluating the deformation at time $t+1$, we obtain

$$[\hat{K}]\{u\}_{t+1} = \{\hat{f}\}_{t+1}, \quad (12)$$

where $[\hat{K}]$ is given as

$$[\hat{K}] = [K] + \frac{\gamma}{\beta \Delta t} [C] + \frac{1}{\beta \Delta t^2} [M] \quad (13)$$

and $\{\hat{f}\}_{t+1}$ is given as

$$\begin{aligned} \{\hat{f}\}_{t+1} = \{f\}_{t+1} + [C] & \left\{ \frac{\gamma}{\beta \Delta t} \{u\}_t + \left(\frac{\gamma}{\beta} - 1 \right) \{\dot{u}\}_t + \left(\frac{\gamma}{2\beta} - 1 \right) \Delta t \{\ddot{u}\}_t \right\} \\ + [M] & \left\{ \frac{1}{\beta \Delta t^2} \{u\}_t + \frac{1}{\beta \Delta t} \{\dot{u}\}_t + \left(\frac{1}{2\beta} - 1 \right) \{\ddot{u}\}_t \right\}. \end{aligned} \quad (14)$$

In the above equation the force vector $\{f\}_{t+1}$ consists of two components. One component is the applied external load on the geometry $\{f\}_{t+1}^{\text{ext}}$ which can be easily evaluated for time $t+1$ based on the applied loading condition. The other component of the force is the interaction force from the fluid $\{f\}_t^{\text{int}}$ which is evaluated for time t . The stiffness matrix $[\hat{K}]$ is invariant in time. Iterative solvers are used to solve the system.

It should be noted that unlike other previous implementations of the coupled LBM-FEM [19, 20] techniques, here the complex nature of the porous geometry requires a different approach. In the previous implementations, FEM was used to model the deformation of individual particles in shear flow of suspensions. The relatively simple geometry of particles allowed for an approach where the effective stiffness matrix $[\hat{K}]$ could be constructed and inverted once at the start of the simulation. In the subsequent timesteps, the matrix–vector product of the inverted stiffness matrix $[\hat{K}]^{-1}$ and the updated force vector $\{\hat{f}\}_{t+1}$ result in the displacement vector $\{u\}_{t+1}$. This computation is performed for each particle in the domain.

In the case of a porous media, the geometry is more complex as shown in Figure 13. Inverting and storing the effective stiffness matrix $[\hat{K}]$ is not feasible. Instead the developments in parallel iterative scheme should be used to solve the system of equations given as (12). Thus, an approach where the geometry could be divided into smaller subdomains, followed by using parallel vector and matrix data structures to assemble the equations and using parallel iterative schemes to solve them would ideally suit this problem.

Fluid–solid coupling

The ‘link-bounce-back’ boundary condition for momentum transfer between the fluid and solid phase in LBM framework has been validated and well established [17, 21, 22]. Here the ‘link-bounce-back’ boundary condition applied along the boundary links as implemented by MacMeccan *et al.* [19] is used. The boundary links cross the surface of the solid boundary and have one end in the fluid and the other in the solid region. The bounce-back boundary conditions assumes the boundary to lie at the mid-point of a boundary link, hence boundary of the solid is captured in a discrete manner.

A ray-tracing algorithm [23] is used to project rays from the lattice nodes along the lattice link directions onto the surface triangles of the solid to determine the intersection. The algorithm provides a fast way to identify links crossing the boundary surface.

The momentum transferred from the fluid to the solid along a single boundary link is given as

$$\delta P_k = 2e_k \left[f_k(\mathbf{x}, t_+) + \rho \frac{w_k}{3} \mathbf{v}_b \cdot \mathbf{e}_k \right], \quad (15)$$

where $f_k(\mathbf{x}, t_+)$ is the fluid distribution at \mathbf{x} after the collision operation represented by t_+ . \mathbf{v}_b is the velocity of the boundary at the link, \mathbf{e}_k is the direction along the boundary link. A simple

linear interpolation scheme is used to transfer the momentum to the finite element nodes. The momentum δP_k is weighted according to the its distance from the point of intersection with the finite element surface to the finite element node as

$$W_j = \frac{d_j}{\sum_{j=1}^3 d_j}, \quad (16)$$

where d_j is the distance from the point of intersection of the link with the finite element surface to the j th finite element nodes.

The fluid distribution in the nodes connected by the boundary link is updated as

$$f_{k'}(\mathbf{x}, t+1) = f_k(\mathbf{x}, t_+) + \rho \frac{w_k}{3} \mathbf{v}_b \cdot \mathbf{e}_k, \quad (17)$$

where k' represents the direction opposite to k .

The presence of two different grids, i.e the Lattice–Boltzmann grid for the fluid phase and the finite element grid of the solid phase introduces a parameter l_{fea} that is defined as the ratio of average finite element edge length to the Lattice–oltzmann grid spacing e_k (MacMeccan *et al.* [19]. Owing to the linear interpolation of momentum onto the finite element nodes, the length scale l_{fea} cannot be less than 1.0. In this work, $l_{\text{fea}} > 2$.

Contact modeling

As the porous media deforms the pores shrink and various surfaces in the solid come in contact. In such a case, it is necessary to model the contact mechanics that occur at the pore scale. The model should be able to capture the contact physics with sufficient accuracy and at the same time should be computationally light enough to solve the numerous contacts that occur during the deformation of a soft porous media. The traditional methods in solid mechanics to model contact such as the penalty method have high computational requirements due to the need to model the contact surfaces using different elements. In the case of porous media due to the enormous number of contacts occurring during deformation, such a method would make the computations unfeasible.

Ding and Aidun [22] developed a near contact model to simulate the interaction of smooth spherical particles based on lubrication forces for approaching spheres. MacMeccan *et al.* [19] extended the model to simulate contact between finite element surfaces. They used short-ranged link-wise force, the magnitude and direction of which depends on the gap between the contacting surfaces. An exponentially increasing repulsive force [24] is also added to the lubrication force to keep the particle surfaces from overlapping. In this work, the near contact model as implemented by MacMeccan *et al.* [19] is used with modifications for use on porous geometries.

The magnitude of the link-wise force is given as

$$\delta F_k = \begin{cases} 0 & \text{if } g > g_c, \\ \frac{3q}{2c_k^2 \lambda} v \rho \left(\frac{1}{g^2} - \frac{1}{c_k^2} \right) \mathbf{U}_a \cdot \mathbf{e}_k, & g_c < g < c_k, \\ \frac{3q}{2c_k^2 \lambda} v \rho \left(\frac{1}{g^2} - \frac{1}{c_k^2} \right) \mathbf{U}_a \cdot \mathbf{e}_k + A_c \exp \left(\frac{-g + g_c}{\sigma_c} \right), & 0 < g < g_c, \end{cases} \quad (18)$$

where \mathbf{U}_a is the approach velocity of the interacting surfaces, g is the link-wise gap between surfaces, g_c is the constant cutoff distance, λ is the local surface curvature and q is chosen to be 0.6 [22]. The parameters g_c and σ_c are dependent on the surface roughness of the geometry and are chosen *a priori*. A_c is chosen such that the repulsive contact force scales appropriately with the applied stresses (σ) i.e. $A_c = \sigma/a_o$, where a_o is the contact area that varies with the applied stress. Based on the applied loading σ and a_o can be determined before hand.

The curvature λ is calculated as

$$\lambda = \frac{1}{N} \sum_{i=1}^N \left| \frac{dT_s}{ds} \right|, \quad (19)$$

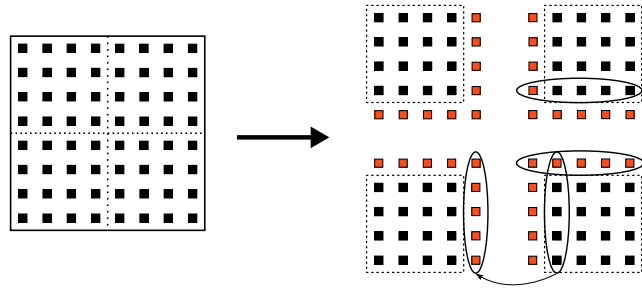


Figure 2. Decomposition of a 2D Lattice-Boltzmann domain into four subdomains for parallel processing. The lattice nodes represented in a different shade ghost nodes. At each time step distributions from the real nodes of one subdomain are communicated to the ghost nodes of the adjacent subdomain as shown in the the figure.

where T_s is the tangent vector to the surface in the direction of s , and s is a vector connecting finite element surface centroids. The summation is performed over all neighbouring surfaces, with $N=3$ for triangles.

The magnitude of interaction force calculated in Equation (18) is added to the surface nodes of the interacting surfaces along with the fluid force given in Equation (15). Thus, the magnitude total force acting on a link connecting approaching surfaces is

$$F_k = \delta P_k + \delta F_k. \quad (20)$$

The force F_k is transferred to the surfaces nodes as mentioned earlier. Subsequently, the force vector for time $t+1$ is updated and solved.

LBM-FEM computations in parallel

Direct numerical simulations demand high computational resources. In modeling saturated porous media, the fluid and solid phases are tightly coupled and need to be solved simultaneously. In addition the complex geometry of the porous media require high spatial and temporal resolutions. This necessitates using distributed computing to obtain results in a realistic time frame.

The parallel algorithm used in this work uses separate ranks to perform fluid and solid calculations. The ranks used for fluid calculations are called ‘fluid ranks’ and those used for solid calculations are called ‘solid ranks’. The method and data structures used for parallelizing and communicating information within and across fluid and solid ranks are described below.

Parallelizing LBM. According to Lattice-Boltzmann equation (1), the distribution $f_k(\mathbf{x}, t+1)$ at lattice node \mathbf{x} and time $t+1$ is solely dependent on the distribution function at lattice $\mathbf{x} + \mathbf{e}_k$ and at time t . Such local nature of algorithm benefits from a data-parallelism approach.

Data parallelism is achieved by dividing the domain among the available ranks. As shown in Figure 2, upon division the of domain, an extra layer of cells also called ghost cells, is added to each subdomain. These ghost cells facilitate the transfer of information between adjacent subdomains at every timestep, thus maintaining the continuity of the entire domain. The simple nature of computations and low communication required leads to excellent scaling, that is needed for a complex problem of deformation of saturated porous media.

Parallelizing FEM. Typically, parallelizing an FEM consists of dividing the elements in the domain among the ranks and using parallel data structures to store and compute the resulting system of equations (Kwon [25], Liu *et al.* [26]). In this work, the unstructured FE mesh is divided using a k-way graph partitioning algorithm [27] provided by the graph partitioning tool PARMETIS. This results in a non-overlapping division of the domain as shown in Figure 3. Subsequently, parallel vector data structure is used to set up the displacement and force vectors while the sparse parallel matrix structure is used to setup up the combined stiffness matrix. The resulting parallel system



Figure 3. Decomposition of unstructured finite element mesh of a rectangular beam into two subdomains using K-way graph partitioning algorithm provided by PARMETIS.

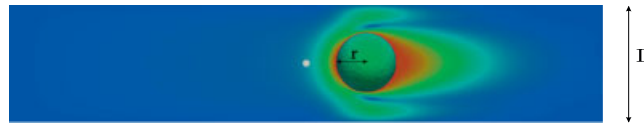


Figure 4. Hindered settling of single solid sphere of radius r in a channel with square cross-section of length L .

of equations are solved using Krylov subspace methods. The libraries provided in the Portable, Extensible Toolkit for Scientific Computations (PETSc [28]) allow for convenient a way of setting up the data structures for parallel vector and matrix computations and also to choose from a variety of parallel iterative solvers.

3. VALIDATION OF METHOD

The method has been validated against the experimental and analytical data for capability in modeling fluid–structure interaction in complex geometries such as a porous media. The problem of settling of sphere in a channel with rectangular cross-section was chosen to test the fluid–structure interaction modeling. In order to test the capability of code to model flow in complex geometries, the problem of flow through a regular arrangement of spheres was chosen. The parallel transient finite element implementation was tested by comparing the wave propagation speed in a rectangular cantilever beam. Finally, the near contact modeling was tested by comparing against the Hertz contact model for deformation of two spheres under compression.

Sphere settling in a rectangular channel

The effect of walls on the settling of a single solid sphere in a rectangular channel has been studied experimentally by Miyamura *et al.* [29]. They obtained the wall correction factor F_w for spheres of different relative radii r^* . The wall correction factor is given as

$$F_w = \frac{v_w}{v_f}, \quad (21)$$

where v_w is the sphere steady-state settling velocity in a channel and v_f is the steady-state settling velocity in a free stream. The relative radii is given as $r^* = r/L$, where r is the radius of the sphere and L is the edge length of the channel as shown in Figure 4.

The above problem of sphere settling in a channel is used as a model problem. Aidun *et al.* [17] found good agreement between the Lattice–Boltzmann simulation of settling of a smooth sphere and the experimental data provided by Miyamura *et al.* Here, the simulations are extended to discretized finite element spheres that are solved in a parallel framework.

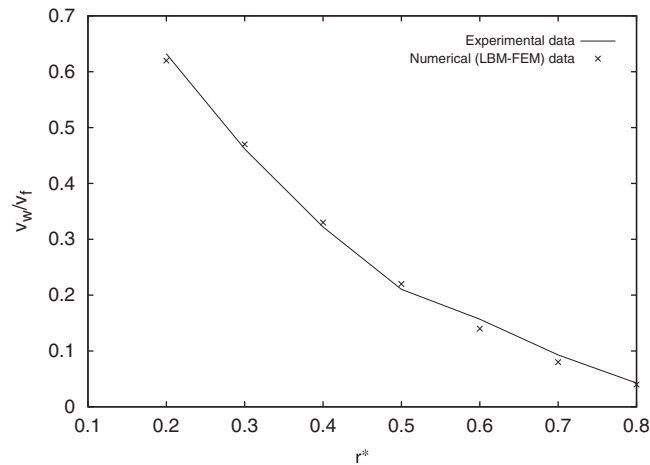


Figure 5. Comparison of the LBM-FEM method with the experimental data for hindered settling of spherical particle in a channel with square cross-section. r^* is the effective radius of the sphere, v_w is the hindered settling velocity of the sphere and v_f is the settling velocity in a free stream.

The boundary conditions are set to bounce-back on the four walls with zero velocity at the inlet (left) and stress free at the outlet (right). The sphere is given a high value of Young's modulus to mimic a rigid sphere. At the start of the simulation, a body force is applied to the sphere and with time allowed to reach a steady-state velocity v_w . The length of channel was set to 400 lattice units and the channel width and height were varied to vary r^* from 0.2 to 0.8. The diameter of the sphere was kept constant ($=40$ lattice units) in all the cases.

Figure 5 shows the comparison of the LBM-FEM method with the experimental data. As can be seen the LBM-FEM results are in good agreement with the experimental data.

Pressure drop across an array of spheres

Analytical models have been proposed [30] to describe the pressure drop across an array of spheres based on modeling the porous media as a bundle of capillary tubes. However, such models underestimate the pressure drop because they do not take into account the energy dissipation in elongation and contraction of fluid elements.

In order to understand flow through porous media Durst *et al.* [31] performed experimental investigations of flow through an array of spheres. The empirical relationship, obtained by Durst *et al.* [31], between pressure drop and fluid velocity for flow through spheres is given as

$$\Omega = 182 + 1.75 Re, \quad (22)$$

where Ω is the friction factor given as $(\Delta P/\Delta L)(D_p/\rho U_0^2)(\varepsilon^3/(1-\varepsilon))Re$ and Re is the Reynolds number given as $U_0 D_p \rho / \mu(1-\varepsilon)$, where D_p is the diameter of spheres, $\Delta P/\Delta L$ is the pressure drop, U_0 is the average velocity, ε is the porosity, ρ and μ are the density and viscosity of the fluid, respectively.

In order to validate the LBM-FEM method to model flow through porous media, we have used the abovementioned experimental results of flow through spheres to compare. The geometry of spheres used in the LBM-FEM validation is shown in Figure 6. Owing to the approximation of the sphere geometry using finite elements the porosity of the arrangement varies such that $0.49 < \varepsilon < 0.51$.

The boundary conditions are periodic along the four walls with a constant uniform velocity profile at the inlet and a stress free or outlet flow boundary condition at the outlet. For a given porosity ε the Reynolds number $Re = U_0 D_p \rho / \mu(1-\varepsilon)$ can be changed by changing the inlet average velocity U_0 or the particle diameter D_p . Since the velocity in Lattice-Boltzmann simulations is limited by the mach number $c_s = 1/\sqrt{3}$, simulations of high Reynolds number are achieved by increasing the

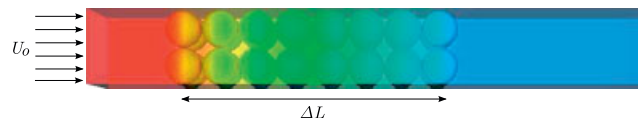


Figure 6. The geometry used to validate Lattice-Boltzmann method to model flow through porous media. The porous media is represented by regular arrangement of spheres. At the inlet (left) a constant velocity U_0 is applied and at the outlet (right) stress-free boundary condition is applied. A periodic boundary condition is applied on the rest of the four walls. The pressure drop across the length ΔL is measured.

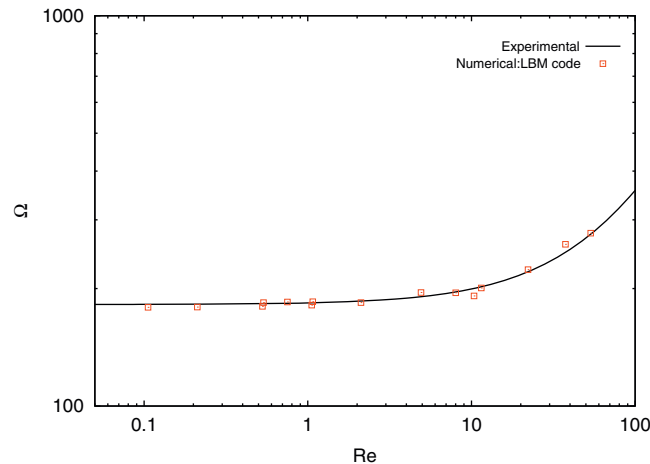


Figure 7. Comparison of the LBM-FEM method with the experimental data for pressure drop in flow through an array of spheres. Ω is friction factor given as $(\Delta P/\Delta L)(D_p/\rho U_0^2)(\varepsilon^3/(1-\varepsilon))Re$ and Re is the Reynolds number given as $U_0 D_p \rho/\mu(1-\varepsilon)$, where D_p is the diameter of spheres, $\Delta P/\Delta L$ is the pressure drop, U_0 is the average velocity, ε is the porosity, ρ and μ are the density and viscosity of the fluid, respectively.

sphere diameter. In lattice units, the diameters of particles chosen in these simulations are 40, 80, 160 and 320. The minimum particle diameter chosen is twice what Bernsdorf *et al.* [32] showed to be sufficient for obtaining results within 3% of experimental value in similar simulations of flows through spheres.

Figure 7 shows the comparison of the LBM-FEM method with the experimental data for pressure drop in flow through an array of spheres. As can be seen the results of LBM-FEM method match closely with the experimental correlation developed by Durst *et al.* The value of the friction coefficient Ω is found to be very sensitive to the volume of spheres V_s and thus in turn on the porosity ε . In the current simulations, the geometry of the sphere is described by triangular surface elements. Such a representation introduces uncertainty in the exact location of boundary for the application of ‘standard-bounce-back’ (SBB) scheme. Thus, there are some differences between the volume of the finite element-meshed geometry of spheres and the Lattice-Boltzmann volume of spheres, which may attribute to the slight difference between the numerical simulation results and the experimentally obtained empirical data.

The results shown above validates the use of SBB boundary condition to model no-slip condition on the walls of solid geometry and accurately predict the energy losses due to both shear and elongational strains. Pan *et al.* [33] have done extensive work to evaluate the accuracy and efficiency of single and multiple relaxation schemes; of first-order and second-order boundary conditions and mesh resolutions. They show that the SBB scheme provides accurate prediction of permeability in porous media flows, if the relaxation parameter (τ) and LBM mesh resolution have been chosen appropriately. Particularly, they show that if $\tau=1$ and the sphere radius is 11.8 LBM units the permeability predictions are accurate.

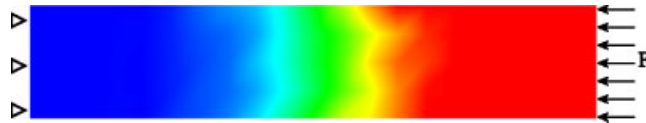


Figure 8. Wave propagation in a rectangular beam. The beam is fixed at the left and is applied a compressive load on the right end. The color represents the stress distribution in the beam.

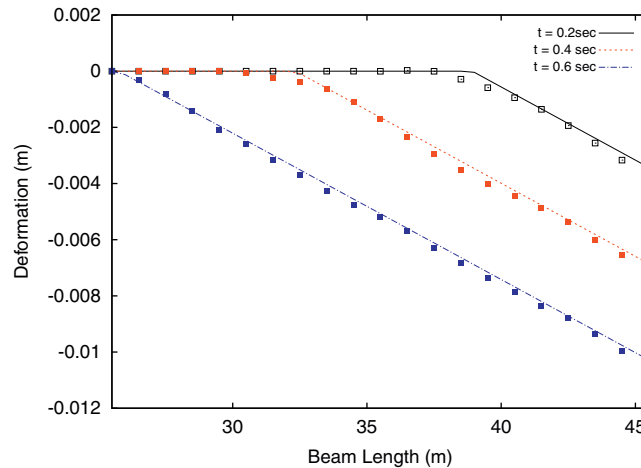


Figure 9. Comparison of deflection $u(x, t)$ obtained from FE analysis with the analytical deflection given in Equation (23). The lines represent the analytical data and the points represent data from FE simulations. The abscissa represents the length along the axis of the cantilever beam.

Wave propagation in a beam

In order to test the transient finite element implementations for accurately modeling time-dependent response of solid, the method was tested against the problem of wave propagation in a beam. A compressive load $F(t)$ is applied to a rectangular cantilever beam as shown in Figure 8. In this case, the load is a step function that remains constant after time $t = 0$. No mass or stiffness damping is used, so as to capture all the modes during the wave propagation. The element edge length was chosen to be equal to $\omega/\delta t$, where ω is the wave speed and δt is the timestep. The deformation response $u(x, t)$ for this problem is given as

$$u(x, t) = \begin{cases} 0 & \text{if } x < \omega t, \\ \frac{F(x - \omega t)}{EA} & \text{if } x > \omega t, \end{cases} \quad (23)$$

where F is the applied compressive load, E is Young's modulus, A is the cross-section area. Figure 9 shows the comparison of the numerical results with the above equation. As can be seen the wave propagation speed is accurately predicted by the FEM.

Comparisons with the Hertz contact model

Hertz solved the problem of contact between two frictionless spherical bodies within elastic limit [34]. The analytical expression for the relative displacement of the centers of two spheres α compared to their non-deformed configuration is given as

$$\alpha = \left[6 \frac{(1 - \nu^2)}{E} \frac{P}{\sqrt{R}} \right]^{\frac{2}{3}}, \quad (24)$$

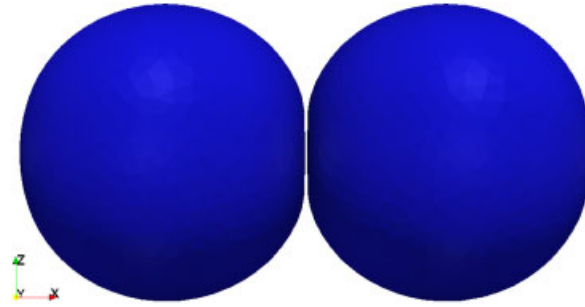


Figure 10. Two spheres are brought into contact by applying a body force along the direction of line joining their centers.

where P is the applied load, R is the radius of both spheres, E is Young's modulus and ν is the Poisson ratio.

The above analytical model was used to test the contact model implemented in the LBM-FEM method. Equation (18) gives the contact model implemented in the LBM-FEM method. As mentioned in methodology, the repulsive contact force is applied along the direction of contact links onto the finite element nodes on the surface of solid geometry. Such a contact model avoids the extensive computational requirements needed by a more rigorous contact model such as the Penalty model but at the same time captures the physics involved during the process of mechanical contact at a small premium of accuracy.

The model problem used to test contact is shown in Figure 10. Two spheres of same radius are made to align along the x -axis. One of the spheres (left) is fixed at the center while the other (right) is free to move along the x -axis. A force P is applied on the sphere free to move. When the spheres reach a steady state the relative displacement of the center of spheres is calculated. The diameter of spheres used in these simulation is 40 lattice units.

The finite element mesh resolution was investigated using two different meshes, as shown in Figure 11. The coarse mesh has a l_{fea} ratio of 4 and the fine mesh has 2. Note that the diameter of the sphere is the same in both cases, thus in the fine mesh, the number of finite elements is large. The contact parameters corresponding to Equation (18) are chosen to provide a repulsive force that scales with the applied stress.

For spheres with ratio $l_{fea}=4$, the plot shows good qualitative behavior, although the deformations are underpredicted compared to the Hertz contact model by about 30%. This shows that the close range interaction model implemented in the numerical method works well to predict the general behavior even with a relatively coarse finite element mesh. The deformation α for ratio $l_{fea}=2$ matches with the Hertz contact model closely. We see that the difference between the Hertz model and numerical results increases at higher deformations, which is predictable since Hertz contact model is only applicable for small deformations. Even with the difference, the numerical method predicts the deformations within 9% of Hertz contact model. Particularly, for small deformations ($\alpha < 0.8$) the match between numerical results and Hertz model is near perfect as shown in the Figure 12.

SIMULATION OF SATURATED DEFORMABLE POROUS MEDIA

The versatility, robustness and efficiency of the method are demonstrated by simulating the compression of a model saturated porous medium. The porous medium used in this simulation consists of a regular arrangement of spheres as shown in Figure 13(a). The diameter of the spheres is 40 lattice units. The element size chosen to discretize the spheres in space is given by $l_{fea}=4$, which is same as the coarse mesh chosen in the validation of contact model. Owing to the approximation of the sphere geometry using finite elements the porosity (ε) is slightly lower than the porosity for a Simple Cubic (SC) arrangement ($\varepsilon \approx 0.49$). The non-dimensional parameter ρ^* , which

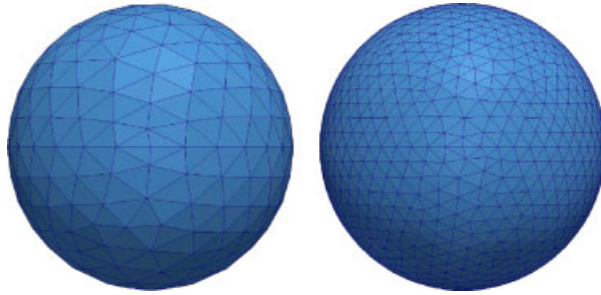


Figure 11. Finite element meshes chosen to test the contact model.

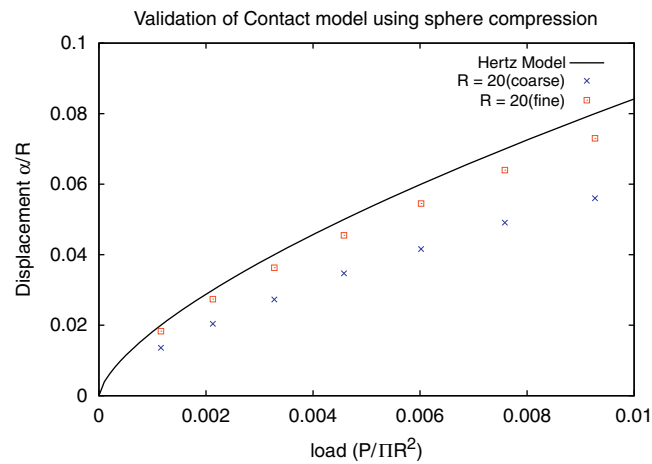


Figure 12. Comparison of the Hertz contact model with the repulsive force model implemented in LBM-FEM method. α represents the deformation due to the compressive load P and R is the radius of the sphere.

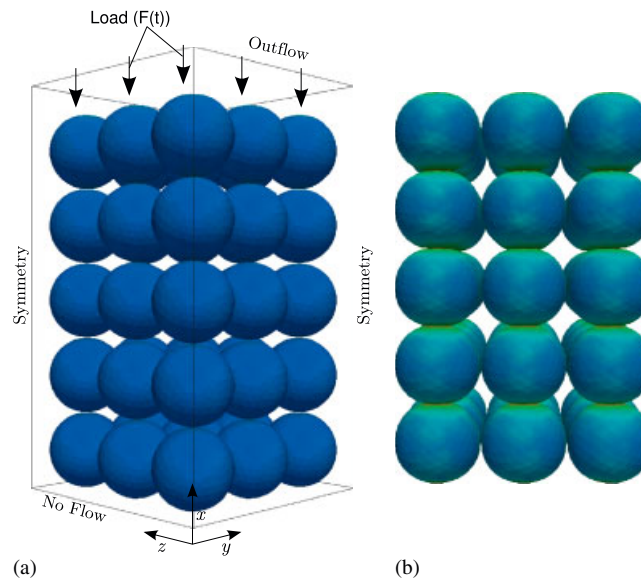


Figure 13. (a) Model saturated porous medium made up of regular arrangement of spheres. Also shown are boundary conditions for the fluid and the loading direction for the solid phase and (b) The configuration of the porous medium at steady state. The color represents strain.

Table I. Values of parameters used in saturated deformable porous media simulation.

E	47.02 MPa
ε	0.49
ρ^{FR}	1000 kg/m ³
ρ^{SR}	2000 kg/m ³
μ_f	4.0 Pa s
$f(t)$	0.01677 kN/m ²

represents the ratio of solid density (ρ_s) to the fluid density (ρ_f) is chosen to be 2.0. Further, the non-dimensional parameter Reynolds number (Re) and Capillary number (Ca) are given as

$$Re = \frac{U_{avg}^F d_p}{\nu^F}, \quad Ca = \frac{\dot{\varepsilon} \mu^F}{E_{avg}} \quad (25)$$

are chosen to be very small ($Re, Ca \ll 1$). In the above equations U_{avg}^F is the average flow velocity in the porous media and ν^F is the fluid kinematic viscosity, $\dot{\varepsilon}$ is the strain rate and E_{avg} is the average bulk modulus of the media. The values of the dimensional parameters used in the simulation are listed in Table I.

The boundary conditions for the problem are also shown in Figure 13(a). For fluid, a symmetry boundary condition is applied along the $x-y$ and $x-z$ sides of the domain. At the top, an outflow or stress-free boundary condition is applied and at the bottom a no-flow boundary is applied. For the solid phase, the nodes near the $x-y$ and $x-z$ walls are constrained to move only in the vertical direction. The nodes at the bottom are constrained to not allow any movement in vertical direction. Further, a time-dependent load ($F(t)$) is applied on nodes at the top. In this problem, the Heaviside function is chosen to be the time-dependent load, such that when $t > 0$; $F(t) = P$.

The chosen FE and LB meshing results in a total of 108 K FE-degrees of freedom (DOFs) and 57 000 K LB-DOFs. The problem was run on a single node of a Dell Power Edge 1950 cluster (Steele:Purdue) with each node containing two Quad-core Intel Xeon 2.33 GHz processors and 16 GB of memory. Five core were used for the fluid phase and three for the solid phase. The problem was run to reach steady state. The resulting deformed porous medium is shown in Figure 13(b), where the color represents strain.

Figure 14 shows the average displacement experienced by the nodes at the top of the arrangement with time. The displacement has been normalized using the radius of the spheres R . Time has been non-dimensionalized as $t^* = t\nu/R^2$, where ν is the kinematic viscosity of the fluid. The displacement shows a rapid non-linear behaviour initially but reaches a steady-state value with time. Further investigations are needed to corroborate the method with the established models [35].

Figure 15 shows the variation of pore pressure at $x = 3R$ with time. Pressure has been normalized as $P^* = PR/\mu_f U$, where μ is the dynamic viscosity of the fluid and U is the average velocity of the solid phase. As expected, the pressure increases rapidly initially because of the compression process and with time reduces to zero. The fluctuations seen in the pressure are due to the weakly compressible nature of the Lattice-Boltzmann scheme.

4. CONCLUSIONS

A robust and scalable numerical method based on a coupled LB-FE method has been developed for direct numerical simulations of saturated porous media under external loading conditions. The method has been tested for accuracy and robustness against sample problems. To test the coupling of fluid and solid forces the problem of sphere settling in a square channel was chosen and found to predict the hindered settling function close to the experimental data. To test the ability of the method to model flow in complex geometries such as a porous media, the problem of flow through

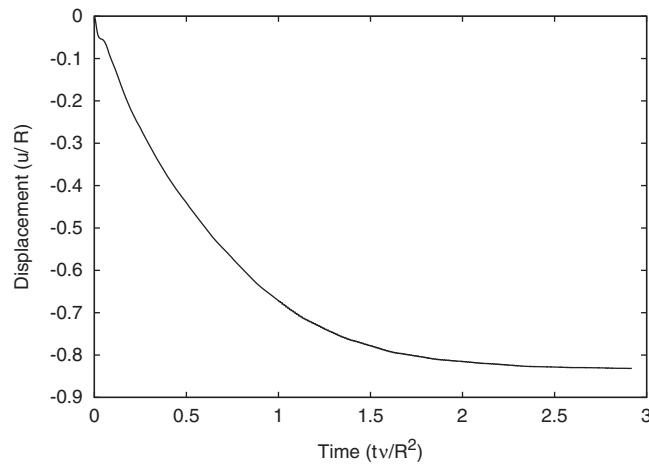
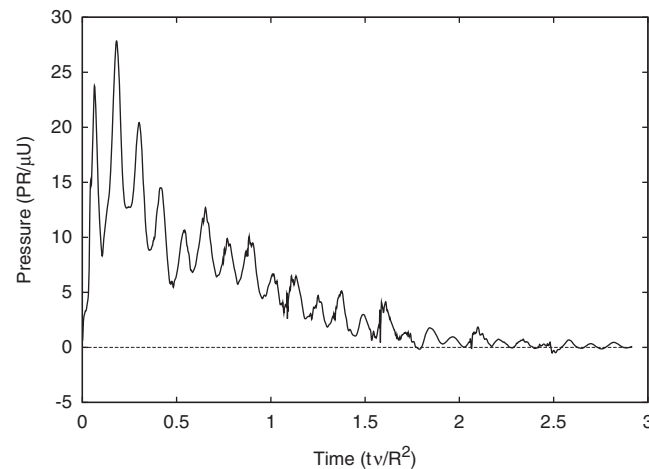


Figure 14. Average normalized displacement w.r.t time.

Figure 15. Average pore pressure w.r.t time ($x=3R$).

array of spheres was chosen. The method showed good agreement with the experimental data. Wave propagation in a cantilever beam was used to test the transient FEM implemented; and found to match the analytical data closely. The contact model implemented in the method was tested against the analytical model presented by Hertz. The results match closely with the analytical model as the mesh resolution is increased, particularly in the small deformation region. Further, a real porous geometry was used for direct numerical simulation of deformation of saturated porous media and the results have been presented.

The LBM-FEM method allows for investigating the behavior of real porous media particularly the effects of non-homogeneous and anisotropic effect. No open parameters were used to match simulation results to experimental or analytical results, thus it captures all the pertinent physics. Further, the local nature of LBM calculations and the advancements in parallel algorithms for FE analysis have allowed for significant scaling opportunities with this method.

Since the method requires an FE mesh as input, there is no limitation on the geometry that can be analyzed with this technique. Thus, the investigations can be extended to other fluid–structure interaction problems involving small deformations. However, in order to avoid singularities and inaccuracies, the FE mesh should be well resolved. For geometries reconstructed through imaging techniques, this is not a trivial task and presents a limitation to analyze such geometries.

Since the method allows for carrying out 'numerical experiments', it provides a convenient way to investigate porous media using granular matter. With this method the authors intend to use granular matter consisting of random and regular arrangement of simple geometries like spheres and cylinders to model the behavior of more complex porous media. Additionally, experiments can be carried out using real porous media to test the validity of the existing homogenization techniques in the field of deformable porous media. Thus, this method can corroborate such techniques by providing improved constitutive relations.

ACKNOWLEDGEMENTS

The authors thank NSF and TERAGRID for providing computational resources to undertake this work. Specifically, the Steele cluster at Purdue and Abe cluster at NCSA have been used for this work. Funding for I. K. is provided through the Institute of Paper Science and Engineering scholarship program.

REFERENCES

1. Biot MA. General theory of three dimensional consolidation. *Journal of Applied Physics* 1941; **12**:155–164.
2. Biot MA. Theory of deformation of a porous viscoelastic anisotropic solid. *Journal of Applied Physics* 1956; **77**(2):182–185.
3. Bowen RM. Incompressible porous media models by use of the theory of mixture. *International Journal of Engineering Science* 1980; **18**:1129–1148.
4. Bowen RM. Compressible porous media models by use of the theory of mixture. *International Journal of Engineering Science* 1982; **20**(6):697–735.
5. de Boer R, Ehlers W. Uplift, friction and capillarity—three fundamental effects for liquid-saturated porous solids. *International Journal of Solids and Structures* 1990; **26**(1):43–57.
6. de Boer R. Highlights in the historical development of porous media theory: toward a consistent macroscopic theory. *Applied Mechanics Review* 1996; **49**:201–262.
7. Ehlers W. On thermodynamics of elasto-plastic media. *Archives of Mechanics* 1989; **41**(1):73–93.
8. Bluhm J. The volume fraction concept in the porous media theory. *Zeitschrift für Angewandte Mathematik und Mechanik* 1997; **77**:1–15.
9. Cancelliere A, Chang C, Foti E, Rothman DH, Succi S. The permeability of a random medium—comparison of simulation with theory. *Physics of Fluids A—Fluid Dynamics* 1990; **2**(12):2085–2088.
10. Soll W, Chen S, Eggert K, Grunau D, Janecky D. Applications of Lattice–Boltzmann/lattice gas techniques to multi-fluid flow in porous media. *Computational Methods in Water Resources* 1994; **99**:991.
11. Ferreol B, Rothman DH. Lattice–Boltzmann simulations of flow through fountainebleau sandstone. *Transport in Porous Media* 1995; **20**:3–20.
12. Boutt DF, Cook BK, McPherson BJOL, Williams JR. Direct simulation of fluid–solid mechanics of porous media using the discrete element and Lattice–Boltzmann methods. *Journal of Geophysical Research* 2007; **112**:B10209.
13. Aidun CK, Clausen JR. The Lattice–Boltzmann method for complex flows. *Annual Review of Fluid Mechanics* 2010; **42**:439–472.
14. Noble DR, Georgiadis GJ, Buckius RO. Comparison of accuracy and performance for Lattice Boltzmann and finite difference simulations of steady viscous flow. *International Journal for Numerical Methods in Fluids* 1996; **23**:1–18.
15. Bernsdorf J, Delhopital F, Brenner G, Durst F. Prediction of pressure losses in porous media using the lattice Boltzmann method. *Proceedings of the International Workshop on Scientific Computing in Chemical Engineering II*, Hamburg, 1999.
16. Breuer M, Bernsdorf J, Zeiser T, Durst F. Accurate computations of the laminar flow past a square cylinder based on two different methods: Lattice–Boltzmann and finite-volume. *International Journal of Heat and Fluid Flow* 2000; **21**:186–196.
17. Aidun CK, Lu Y, Ding EJ. Direct analysis of particulate suspensions with inertia using the discrete Boltzmann equation. *Journal of Fluid Mechanics* 1998; **373**:287–311.
18. Saad Y. *Iterative Methods for Sparse Linear Systems* (2nd edn). SIAM: Philadelphia, PA, 2003.
19. MacMeccan RM, Clausen JR, Neitzel GP, Aidun CK. Simulating deformable particle suspensions using a coupled Lattice–Boltzmann and finite-element method. *Journal of Fluid Mechanics* 2009; **618**:13–39.
20. Sui Y, Chew YT, Roy P, Low HT. A hybrid method to study flow-induced deformation of three-dimensional capsules. *Journal of Computational Physics* 2008; **227**:6351–6371.
21. Ladd AJC. Numerical simulations of particulate suspensions via a discretized Boltzmann equation. Part 1. Theoretical foundation. *Journal of Fluid Mechanics* 1994; **271**:285–309.
22. Ding EJ, Aidun CK. Extension of the Lattice–Boltzmann method for direct simulation of suspended particles near contact. *Journal of Statistical Physics* 2003; **112**(3):685–708.
23. Moller T, Trombore B. Fast, minimum storage ray-triangle intersection. *Journal of Graphics Tools* 1997; **2**:21–28.

24. Buxton GA, Verberg R, Jasnow D, Balas AC. Newtonian fluid meets an elastic solid: coupling Lattice Boltzmann and lattice-spring models. *Physical Review E* 2005; **71**:056707.
25. Hee-Dae K. Efficient parallel implementations of finite element methods based on the conjugate gradient method. *Applied Mathematics and Computation* 2003; **145**:869–880.
26. Liu C-H, Leung YC, Woo C-M. Development of a scalable finite element solution to the Navier Stokes equations. *Computational Mechanics* 1997; **32**:185–198.
27. Karypis G, Kumar V. Multilevel k-way partitioning scheme for irregular graphs. *Journal of Parallel and Distributed Computing* 1998; **48**:10–27.
28. Balay S, Gropp WD, McInnes LC, Smith BF. Efficient management of parallelism in object oriented numerical software libraries. In *Modern Software Tools in Scientific Computing*, Arge E, Bruaset AM, Langtangen HP (eds). Birkhauser Press: Basel (Boston/Stuttgart), 1997; 163–202.
29. Miyamura A, Iwasaki S, Ishii T. Experimental wall correction factors of single solid spheres in triangular and square cylinders, and parallel plates. *International Journal of Multiphase Flow* 1981; **7**:41–46.
30. Bird RB, Stewart WE, Lightfoot EN. *Transport Phenomena* (2nd edn). Wiley: New York, 2002.
31. Durst F, Hass R, Interthal W. The nature of flows through porous media. *Journal of Non-Newtonian Fluid Mechanics* 1987; **22**:169–189.
32. Bernsdorf J, Brenner G, Durst F. Numerical analysis of the pressure drop in porous media flow with lattice Boltzmann (BGK) automata. *Computer Physics Communications* 2000; **129**:247–255.
33. Pan C, Li-Shi L, Cass TM. An evaluation of lattice Boltzmann schemes for porous medium flow simulation. *Computers and Fluids* 2006; **35**:898–909.
34. Timoshenko SP, Goodier JN. *Theory of Elasticity* (3rd edn). McGraw-Hill: New York, 1970.
35. de Boer R, Ehlers W, Lui Z. One-dimensional transient wave propagation in fluid-saturated incompressible porous media. *Archive of Applied Mechanics* 1993; **63**:59–72.